

PAPER • OPEN ACCESS

Increasing the topological diversity of light with modulated Poincaré beams

To cite this article: Pegah Darvehi *et al* 2021 *J. Opt.* **23** 054002

View the [article online](#) for updates and enhancements.



IOP | ebooks™

Bringing together innovative digital publishing with leading authors from the global scientific community.

Start exploring the collection—download the first chapter of every title for free.

Increasing the topological diversity of light with modulated Poincaré beams

Pegah Darvehi¹, Verónica Vicuña-Hernández¹ , Lorenzo Marrucci^{1,2} ,
Ester Piedipalumbo^{1,3} , Enrico Santamato¹ and Bruno Piccirillo^{1,*} 

¹ Dipartimento di Fisica ‘Ettore Pancini’, Università degli Studi di Napoli Federico II, Complesso Universitario di Monte Sant’Angelo, Via Cintia 80126 Napoli, Italy

² CNR-ISASI, Institute of Applied Science and Intelligent Systems, Via Campi Flegrei 34, 80078 Pozzuoli (NA), Italy

³ INFN, Sez. di Napoli, Complesso Universitario di Monte Sant’Angelo, Via Cintia 80126 Napoli, Italy

E-mail: bruno.piccirillo@unina.it

Received 13 January 2021, revised 8 March 2021

Accepted for publication 26 March 2021

Published 21 April 2021



CrossMark

Abstract

We introduce a wide class of singular inhomogeneously polarized beams characterized by a nonuniform rotation rate of the local polarization azimuth about a C- or a V-point. They are obtained by adding an extra phase modulation with an m -fold rotational symmetry to the helical wavefronts underpinning Poincaré beams. The resulting modulated Poincaré beams have been theoretically studied and experimentally generated using tailored space-varying-axis plates based on liquid crystals.

Keywords: optical singularities, optical angular momentum, geometric phase

(Some figures may appear in colour only in the online journal)

1. Introduction

Inhomogeneously polarized light is a ubiquitous phenomenon: many animals can see variations in polarization just as humans see variations in color and the varying pattern of polarized light reflected from their bodies is used as a form of signaling [1]; spatially-varying polarization patterns arise in the speckle fields produced by bulk scattering from molecular configurations in liquid crystals (LCs) [2, 3], cell structures in biological tissues [4], or in gravitational-lensing shear fields [5], just to mention a few. This has fueled interest in better understanding optical maps of polarization, particularly those containing polarization singularities, i.e. points in which one of the parameters specifying the polarization of the light is undefined [6]. Such interest has been further enhanced by the possibility of generating coherent optical beams with spatially varying

polarization distributions over their cross section. Such beams have been exploited in numerous applications to photonics [7, 8], astronomy [9, 10], microscopy [11–13], optomechanics [14, 15], materials structuring [16], nanophotonics [17, 18] and quantum sciences [19–21]. Fundamental properties of inhomogeneously polarized optical beams have been largely studied in the last two decades [22–28]: they correspond to whole regions on the Poincaré sphere and therefore are sometimes called Poincaré beams [29, 30], though such denomination is generally reserved to beams in which the state of polarization varies so as to cover the full Poincaré sphere. The polarization state of inhomogeneously polarized beams (IPBs), in the slow envelope limit, is represented by spatially dependent Stokes parameters, i.e. $S_0(x, y)$, $S_1(x, y)$, $S_2(x, y)$ and $S_3(x, y)$, with x and y being the coordinates in the plane transverse to the propagation direction. The optical fields in which the local polarization state is mainly elliptical, i.e. $S_3(x, y) \neq 0$ almost everywhere in the transverse plane, are commonly named ellipse fields; those in which the local polarization state is mainly linear, i.e. $S_3(x, y) = 0$ almost everywhere, are named vector fields. In ellipse fields, points of undefined ellipse orientation are named C-points [22]. A C-point, in the far field, corresponds to a state of circular polarization, surrounded

* Author to whom any correspondence should be addressed.



Original Content from this work may be used under the terms of the [Creative Commons Attribution 4.0 licence](https://creativecommons.org/licenses/by/4.0/). Any further distribution of this work must maintain attribution to the author(s) and the title of the work, journal citation and DOI.

by a field of ellipses whose orientations rotate clockwise or counterclockwise about it. Such rotation is represented by an integer or half-integer index I_C , indicating that the azimuthal coordinate on the Poincaré sphere rotates $2|I_C|$ times per turn about the singularity. Likewise, in vector fields, points at which the linear polarization orientation is indeterminate are named V-points. Actually, at such points both the polarization azimuth and the handedness are undefined, and hence the field itself must vanish. V-points are surrounded by points that have linear states of polarization with varying azimuth characterized by a rotation index I_V , also known as the Poincaré–Hopf index [31, 32]. Unlike I_C , the rotation index I_V can only take integer values. Ellipse field topology around a C-point is multifarious, even in the simplest case of radially invariant polarization patterns. From C-points, radial polarization lines or L-lines may originate. Along these lines, the orientation of the major axis of the local polarization ellipse, or local polarization azimuth, matches the radial orientation [33, 34]. A number of L-lines may ray out of a C-point depending on the sign of the rotation index I_C and the degree of uniformity of the rate of rotation of the azimuth about the C-point. Basic shapes of the patterns of C-points are lemon ($I_C = 1/2$, 1 radial line), star ($I_C = -1/2$, 3 radial lines) and monstar ($I_C = 1/2$, 3 radial lines). The first two disclinations have symmetric patterns; the last one is asymmetric and occurs when the azimuth rotation rate about a C-point exceeds a threshold value [33], giving rise to a different number of radial lines than lemons or stars with the same I_C index [35, 36].

In the overwhelming majority of cases, the methods adopted to synthesize IPBs are based on the coherent superposition of two distinct spatial modes in two orthogonal polarization states. However, distinct approaches have been exploited depending on the actual tools used for molding wavefronts: sub-wavelength structures [37, 38], stress birefringence [29], interferometer-based superpositions [30, 31, 39–42], q-plates [33, 43, 44]. To date, generating arbitrarily tailored IPBs is difficult, as ideally this requires: (i) determining a pair of spatial modes whose spatially varying phase difference yields the targeted polarization map in the selected polarization basis; (ii) precisely generating the optical beams in those spatial modes; (iii) superimposing such beams in a stable way. In practice, we usually content ourselves with ‘fishing’ our polarization maps out of those that can be practically realized by combining easy-to-generate well-known spatial modes. It is quite challenging to engineer more complex patterns, such as those containing multiple C-points or monstar singularities, which also require being able to manipulate the rotation rate of the polarization azimuth around a C-point.

In this paper, we present a general method for engineering IPBs in which the rotation rate of the local polarization azimuth around a C- or a V-point can be set as desired and realized in practice without resorting to computational approximations. The design procedure capitalizes on the same geometric approach underpinning the generation of free-form dark hollow beams [45]: it enables one to shape the wavefronts of the spatial modes required to generate the target polarization map without passing through the direct manipulation of the orbital angular momentum (OAM) spectrum. Our approach

delivers its full potential through properly designed LC-based spatially varying axes retardation waveplates (SVAPs). The well-known q-plates—which prototype SVAPs—have already proved to be very convenient tools for generating polarization singularities [33, 43, 44, 46]. An SVAP, in fact, can be operated so as to directly imprint the LC optic axis distribution onto the topographic map of the polarization azimuth, over the whole transverse cross section of the transmitted laser beam. No interferometer is needed. This makes our method unique in its straightforward simplicity. The azimuth orientation information is actually encoded in the SVAP in the form of the Pancharatnam–Berry phase. Alternatively, although less conveniently, the same phase could be generated by a spatial light modulator suitably inserted into an interferometric setup. Here, we demonstrate the SVAP-based method for generating exotic polarization-structured beams, with either V-points or C-points on their axis. The resulting beam intensity patterns are also rather complex, including the possible occurrence of transverse amplitude ‘fault lines’, where intensity suddenly vanishes.

The paper is organized as follows. In section 2 we present the theory describing the generation of IPBs with a nonuniform azimuthal rotation rate. In section 3 we illustrate the operation of SVAPs encoding geometric phase distribution with a nonuniform azimuthal dependence and explain how we use them to create various polarization patterns. In section 4 we introduce some examples of such beams and demonstrate their properties on experimental grounds.

2. IPBs with nonuniform rate of rotation of the azimuth

In the paraxial regime, any spatially varying inhomogeneous polarization distribution can be regarded as the superposition of two orthogonal uniform polarization states with a spatially varying phase difference. This suggests that any transverse map of polarization can be obtained by interference between two homogeneously polarized beams in two distinct and conveniently mismatched spatial modes,

$$|IPB\rangle = c_L f_L(r, \phi, z) e^{i\psi_L(r, \phi, z)} |L\rangle + c_R e^{i\alpha} f_R(r, \phi, z) e^{i\psi_R(r, \phi, z)} |R\rangle \quad (1)$$

where a cylindrical coordinates system has been set with z along the propagation direction, $|L\rangle$ and $|R\rangle$ denote left- and right-circular polarization states, respectively, $f_L(r, \phi, z) e^{i\psi_L(r, \phi, z)}$ and $f_R(r, \phi, z) e^{i\psi_R(r, \phi, z)}$ are complex functions describing the normalized scalar modes in the two orthogonally polarized states, c_L and $c_R e^{i\alpha}$ are the coefficients providing the relative contribution of each mode to the overall amplitude and their global phase change. The topological features of the polarization map will depend on the chosen polarization basis states, on the coefficients ratio c_R/c_L and on both the local, $\psi_R(r, \phi, z) - \psi_L(r, \phi, z)$, and global, α , phase differences between the selected spatial modes.

Poincaré and vector modes are nonseparable superpositions of spatial and polarization modes like those in

equation (1). In the past, IPBs have been realized by superposing Hermite–Gaussian modes with orthogonal linear polarization or combinations of high-order Laguerre–Gaussian modes with orthogonal circular polarizations [30], giving rise to different types of polarization singularities. Here, we propose to generate IPBs using nonseparable superpositions of free-form helical (FFH) [45] modes with orthogonal circular polarization.

2.1. FFH modes

An FFH spatial mode of m -order and topological charge ℓ is obtained by subjecting an ℓ -charged helical-phase mode to an additional m -fold rotation-symmetric phase. Examples of the wavefront shapes resulting from such phase combinations are provided in figures 1 and 2. Specifically, an FFH mode can be generated by multiplying an ordinary TEM₀₀ Gaussian mode by the purely azimuthal phase factor [45]

$$e^{i2\Psi(\phi)} = e^{i\ell\vartheta(\phi)}, \quad (2)$$

where ϑ is defined here as the polar angle of the unit vector $\hat{\mathbf{n}} = (n_x, n_y)$, with

$$\begin{aligned} n_x(\phi) &= \cos \vartheta = \frac{\rho \cos \phi + \dot{\rho} \sin \phi}{(\dot{\rho}^2 + \rho^2)^{1/2}}, \\ n_y(\phi) &= \sin \vartheta = \frac{\rho \sin \phi - \dot{\rho} \cos \phi}{(\dot{\rho}^2 + \rho^2)^{1/2}}, \end{aligned} \quad (3)$$

and

$$\rho(\phi) = \left(\left| \frac{\cos \frac{m\phi}{4}}{a} \right|^{n_2} + \left| \frac{\sin \frac{m\phi}{4}}{b} \right|^{n_3} \right)^{-\frac{1}{n_1}}, \quad \dot{\rho} = \frac{d\rho}{d\phi}. \quad (4)$$

By varying the parameters m , n_1 , n_2 , n_3 and a and b , equation (4) represents, in polar coordinates, multiple classes of plane curves $\gamma_m(a, b, n_1, n_2, n_3)$ of the most diverse kinds. It was introduced by the botanist Gielis in 2003, with the name ‘superformula’, to study forms in plants and other living organisms [47]. Specifically ρ is the distance of a point of the curve γ_m from the origin of the coordinate system as a function of the azimuthal angle ϕ , m is an integer number, n_1 , n_2 and n_3 are three integers controlling its local radius of curvature and, finally, the positive real numbers a and b parameterize the radii of the circumferences respectively inscribed and circumscribed to the curve γ_m . For even $m = 2k$, equation (4) describes a curve γ_{2k} closing over the interval $[0, 2\pi)$. Here, γ_{2k} is rotationally symmetric by an angle $2\pi/k$. For odd $m = 2k + 1$, γ_{2k+1} closes over the interval $[0, 4\pi)$. When $a = b$ and $n_2 = n_3$, γ_m exhibits an m -fold rotational symmetry C_m . While varying all the free parameters in equation (4), the generated curves can be very diverse and possibly even develop cusps. It is worth noting that, for $m = 4$, $a = b$ and $n_2 = n_3 > 2$, the superformula simply returns the superellipses first introduced by Lamé in 1818 [48].

According to equation (2), the phase of an FFH mode is hence proportional to the angle $\vartheta(\phi)$ formed by the unit vector $\hat{\mathbf{n}}$ normal to the curve $\gamma_m(a, b, n_1, n_2, n_3)$ with respect to

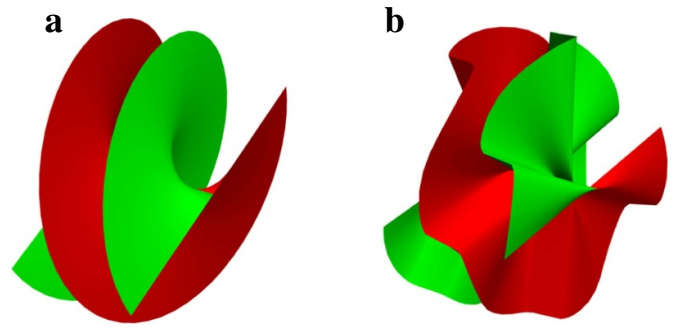


Figure 1. Modulated vs unmodulated helical wavefronts: (a) a uniform helical wavefront for $\ell = 2$ (γ_{∞}); (b) a modulated helical wavefront for $\ell = 2$ and γ_5 ($a = b, n_1 = 1/2; n_2 = n_3 = 4/3$).

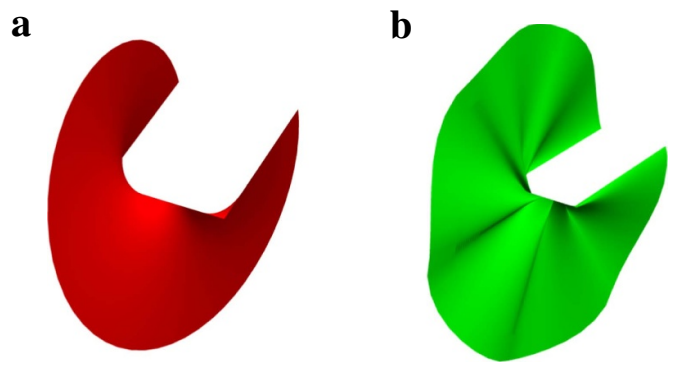


Figure 2. Modulated vs unmodulated helical wavefronts: (a) a uniform helical wavefront for $\ell = 1$ (γ_{∞}); (b) a modulated helical wavefront for $\ell = 2$ and γ_6 ($a = b, n_1 = 2/3; n_2 = n_3 = 2.3$).

a specified reference axis x . An ℓ -charge m -order FFH mode obviously does not carry a well-defined OAM and its spectrum includes multiple indices reflecting the m -fold rotational symmetry of the generating curve. To determine such indices, it is convenient to express the phase $\Psi(\phi)$ in equation (2) as follows

$$\begin{aligned} e^{i2\Psi(\phi)} &= (n_x + i n_y)^\ell = \left[\frac{\rho(\phi) - i\dot{\rho}(\phi)}{\rho(\phi) + i\dot{\rho}(\phi)} \right]^q \\ e^{i2q\phi} &= e^{iq\bar{\psi}(\phi)} e^{i2q\phi}, \end{aligned} \quad (5)$$

where we set $q = \ell/2$. Here, q is hence integer or half-integer depending on whether ℓ is even or odd, respectively. The FFH phase factor therefore can be separated into the product of the helical background phase factor $e^{i\ell\phi} = e^{i2q\phi}$ times the modulation phase factor $e^{iq\bar{\psi}(\phi)}$. The latter is a periodic function of ϕ with period $2\pi/m$, i.e.

$$e^{iq\bar{\psi}(\phi + \frac{2\pi}{m})} = e^{iq\bar{\psi}(\phi)}, \quad (6)$$

and hence can be expanded in a Fourier series

$$\begin{aligned} e^{iq\bar{\psi}(\phi)} &= \sum_h \chi_h e^{ihm\phi}, \\ \chi_h &= \frac{m}{2\pi} \int_0^{\frac{2\pi}{m}} \left[\frac{\rho(\phi) - i\dot{\rho}(\phi)}{\rho(\phi) + i\dot{\rho}(\phi)} \right]^q e^{-ihm\phi} d\phi. \end{aligned} \quad (7)$$

Then, the OAM spectrum of an ℓ -charge m -order FFH beam turns out to include only the components with indices $\ell \pm hm$, with h being any integer and $\ell = 2q$ the OAM index corresponding to the background helical mode. The azimuthal phase factor in equation (2) can be finally expressed as the following helical mode expansion

$$e^{i2\Psi(\phi)} = \sum_h \chi_h e^{i(2q+hm\phi)} = \sum_l c_l e^{il\phi}, \quad l = 2q + hm. \quad (8)$$

The mean value of the OAM in an m -order FFH mode can be easily calculated from equations (2) and (3),

$$\begin{aligned} \langle L_z \rangle &= -\frac{i\hbar}{2\pi} \int_0^{2\pi} e^{-i2\Psi(\phi)} \frac{\partial}{\partial \phi} e^{i2\Psi(\phi)} \\ &= \frac{\hbar}{\pi} \Psi(\phi)|_0^{2\pi} = \frac{\hbar}{\pi} q \vartheta(\phi)|_0^{2\pi} = 2\hbar q. \end{aligned} \quad (9)$$

This result indicates that the mean OAM carried by an ℓ -charge FFH mode is always $\hbar\ell = 2\hbar q$ per photon, independently of m . It is therefore coincident with the OAM per photon of the background helical mode and it is proportional to the overall topological charge of the transverse wavefront. The phase modulation factor $e^{iq\varphi(\phi)}$ defined in equation (5) has a zero mean OAM. However, the specific value of the fraction $|c_l|^2$ of the total power of the optical field carrying an OAM proportional to l depends on the geometric details of the generating curve $\gamma_m(a, b, n_1, n_2, n_3)$ and ultimately on the specific values of the parameters in equation (4). Uniform helical modes can be easily obtained as a special case of FFH modes when the generating curve γ_m degenerates into a circumference ($\gamma_m \rightarrow \gamma_\infty$).

Phase profiles of ℓ -charge m -order FFH modes have the following remarkable symmetry properties:

- for odd ℓ (half-integer q), the phase profile is invariant under combined charge inversion and reflection across the x axis;
- for even ℓ (integer q) and even m , the phase profile is invariant under combined charge inversion and reflection across either the x or y axis;
- for even ℓ and odd m , the phase profile is again invariant only under combined charge inversion and reflection across the x axis.

Owing to diffraction, the rotational symmetry of the FFH modes encapsulated in their phase modulation also affects the intensity profile of the generated beam. In general, light intensity is expected to be equally partitioned among the m equally spaced sectors of the phase profile [45], giving rise to m -fold rotationally invariant dark hollow beams, some examples of which are shown in figures 10 and 11. When the azimuthal phase modulation includes discontinuities (due to cusps in the superformula curve γ_m), the intensity pattern may show the appearance of ‘fault lines’ of vanishing intensity even in the near field, i.e. after an infinitesimal propagation length, as shown in figures 8 and 9.

Free space propagation obviously alters the shape of FFH modes, but it does not influence their symmetry properties.

2.2. Modulated Poincaré beams

A wide class of inhomogeneously polarized optical beams can be obtained by setting the two spatial modes in equation (1) to FFH modes, i.e.

$$\begin{aligned} |MPB(m_1, q_1, \xi_1; m_2, q_2, \xi_2)\rangle &= c_L \text{FFH}_{q_1}^{m_1}(\xi_1)|L\rangle \\ &+ c_R e^{i\alpha} \text{FFH}_{q_2}^{m_2}(\xi_2)|R\rangle, \end{aligned} \quad (10)$$

where $\text{FFH}_{q_i}^{m_i}(\xi_i)$ denotes the m -order FFH mode of topological charge $2q_i$, corresponding to the set of parameters $\xi_i = (a_i, b_i, n_{1i}, n_{2i}, n_{3i})$. The beams are here dubbed ‘modulated Poincaré beams’ (MPBs), since they can be regarded as a generalization of ordinary Poincaré beams to the case of nonuniform azimuthal rotation rate of the polarization ellipses.

To discuss the features of the polarization maps of such MPBs let us consider here a couple of simpler examples. Suppose e.g. that, in the transverse plane at $z=0$, both modes have the same Gaussian radial profile $E_0 e^{-r^2/w_0^2}$, but the left-polarized mode has $\ell_1 = 2q_1 = 0$, while the right-polarized mode has $\ell = 1$ ($q_2 = 1/2$). When $c_L = c_R = 1$ and $\alpha = 0$, the polarization map at $z=0$ (near field), for any ϕ , turns out to be linearly polarized along the local direction of the unit vector \hat{n} normal to the curve $\gamma(m_2, \xi_2)$ generating $\text{FFH}_{q_2}^{m_2}(\xi_2)$. In this case, in fact, according to equation (2), the local phase difference between $|L\rangle$ and $|R\rangle$ coincides with the phase factor $e^{-i\vartheta(\phi)}$. A possible non-vanishing global phase α leads only to an additional uniform rotation of the polarization orientation by the same angle. In propagation the field becomes an ellipse one, while maintaining the same topology. At the center, the beam will have a C-point with a rotational index $I_C = q_2 = 1/2$.

As a second example, if we take $m_1 = m_2$, $\xi_1 = \xi_2$, but $q_1 = -q_2$, the polarization at $z=0$ turns out to be linearly polarized everywhere along a local direction that forms an angle $2\vartheta(\phi)$ with respect to the x axis. In this case, in the far field the field remains a vector one, with a central V-point that has a rotational index $I_V = -2q_1 = 2q_2$.

In these examples, the geometrical properties of the generating curves directly map onto the topological properties of the resulting beam polarization distribution. This simple relationship turns out to be very useful in tailoring the rotation rate of the local azimuth of the polarization patterns of the beams described by equation (10). The ability to tailor the azimuthal rotation rate of polarization about a singular point, as mentioned above, has great potential for both fundamental and application purposes.

3. Generation of MPBs through free form azimuthal SVAPs

The operation principle of SVAP devices has already been described elsewhere [44, 49–51]. In particular, the optical effect of a generic free-form azimuthal SVAP can be described by the operator $\hat{Q}(q, m, \xi)$ acting on the local polarization state of the field, defined as

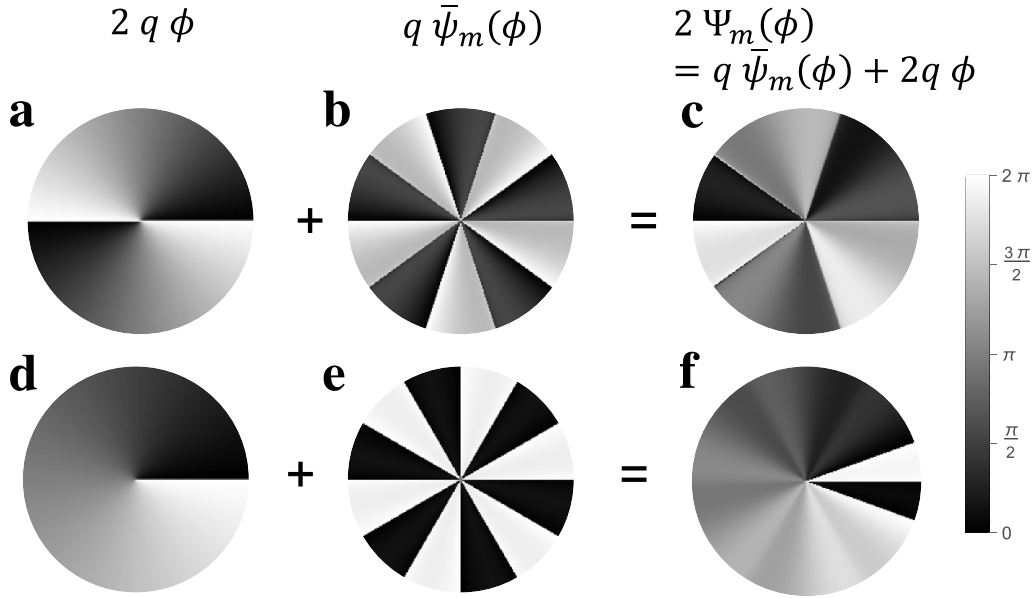


Figure 3. Phase profiles of starfish and water primrose FFH modes: (a) background phase profile 2ϕ ($q = 1$); (b) starfish phase modulation $\bar{\psi}_5(\phi)$ generated from $\gamma_5(a = b, n_1 = 1/2, n_2 = n_3 = 4/3)$; (c) total starfish phase $2\Psi_5(\phi) = \bar{\psi}_5(\phi) + 2\phi$; (d) background phase profile ϕ ($q = 1/2$); (e) primrose phase modulation $\bar{\psi}_6(\phi)$ generated from $\gamma_6(a = b, n_1 = 2/3, n_2 = n_3 = 2.3)$; (f) total primrose phase $2\Psi_6(\phi) = \bar{\psi}_6(\phi) + \phi$.

$$\hat{Q}(q, m, \xi) = \cos \frac{\delta}{2} (|L\rangle \langle L| + |R\rangle \langle R|) + i \sin \frac{\delta}{2} \left(e^{i2\Psi(\phi; q, m, \xi)} |R\rangle \langle L| + e^{-i2\Psi(\phi; q, m, \xi)} |L\rangle \langle R| \right), \quad (11)$$

in which the Pancharatnam–Berry phase factor $e^{i2\Psi(\phi; q, m, \xi)}$ is defined by equations (2)–(5) and δ is the birefringent phase retardation of the device, allowing its tunability.

Our LC SVAPs have been fabricated by adopting a ‘direct-write approach’ to pattern the LC anchoring to the ITO-coated glass walls of the cell. Electrical control of the retardation δ —or electrical tunability—and non-diffractive operation are just some of the main advantages of this technology.

Let us consider two specific operation modes of these devices. In the first case, the SVAP retardation is set to $\delta = \pi/2$ (quarter-waveplate operation) and the input light is a circularly polarized Gaussian beam. In this case, if the input polarization is left circular, the SVAP output is an MPB with $q_1 = 0, q_2 = q, m_2 = m, \xi_2 = \xi$ and $c_R/c_L = 1$. The global phase is $\alpha = \pi/2$. In the near field, the resulting MPB then has a linear polarization map just point-by-point coincident with the SVAP optic axis distribution (except for a $\pi/2$ rotation due to the global phase), with a central C-point of index $I_C = q$, as discussed in the previous section. Similar behavior is obtained with an input right-circular polarization. A further possible variant of the obtained polarization map can then be obtained by letting the MPB pass through a half-waveplate, thus exchanging left and right circular components.

In the second operation mode, the SVAP retardation is set to $\delta = \pi$ (half-waveplate operation) and the input polarization is linear. In this case the SVAP generates an MPB with

$-q_1 = q_2 = q, m_1 = m_2 = m$ and $\xi_1 = \xi_2 = \xi$, leading to a vector field with a central V-point with $I_V = 2q$. The MPB vector field is of course also dependent on the input linear polarization orientation, which introduces a further local rotation of the polarization by a uniform angle.

We shall see in the following specific examples of these various operating modes for specific examples of SVAP geometries.

4. Topological diversity of MPBs

To provide the readers with a glimpse of the wide variety of possible MPBs that can be generated by SVAP devices, here we analyze in detail two SVAP geometries, differing in their charge q , order parity $(-1)^m$ and azimuthal modulation strength as determined by the choice of parameters ξ . The modulation strength is in turn determined by the local curvature of the generating curve $\gamma_m(a = b)$, as fixed by the parameters n_1 and $n_2 = n_3$ in equation (4).

4.1. Selection and generation of scalar FFH_q^m modes via SVAPs

We consider the MPBs generated by either the ‘starfish’ modes FFH_{±1}⁵ ($a = b, n_1 = 1/2, n_2 = n_3 = 4/3$) or the ‘water primrose’ modes FFH_{±1/2}⁶ ($a = b, n_1 = 2/3, n_2 = n_3 = 2.3$). The starfish and primrose phase profiles are shown in figures 3(c) and (f). Each profile has been represented as the sum of the corresponding background helical phase (figures 3(a) and (d)) and modulation contribution (figures 3(b) and (e)).

The resulting azimuthal wavefronts at $z = 0$ (see equation (5)) are sketched in figures 1(b) and 2(b), respectively.

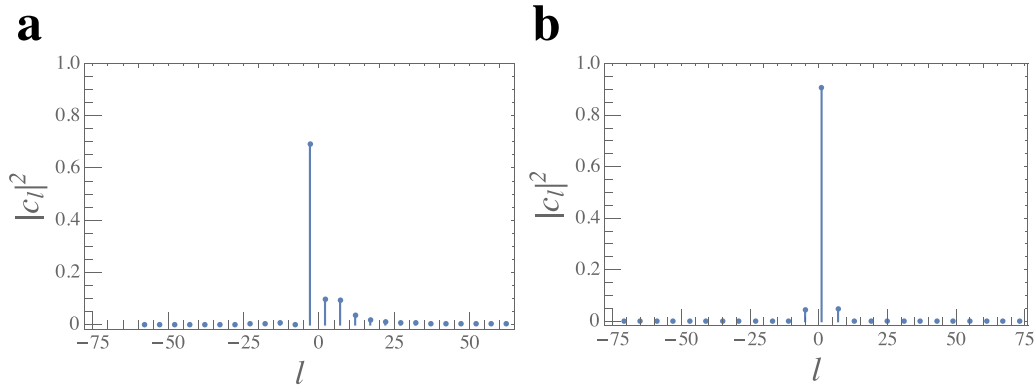


Figure 4. OAM power spectra for starfish (a) and primrose (b) FFH modes.

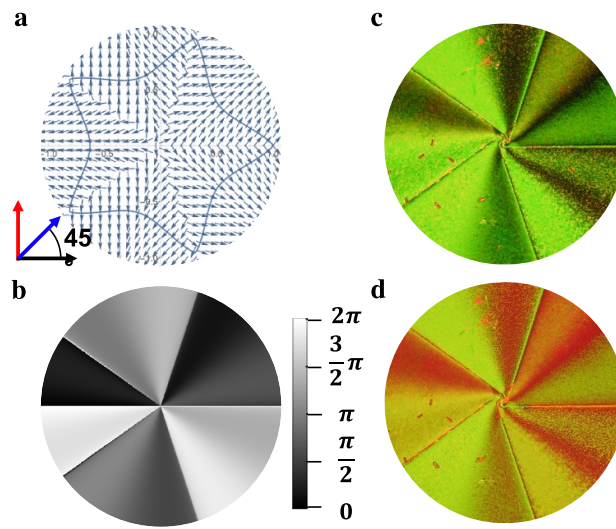


Figure 5. Experimental observation of the optic axis distribution of the starfish SVAP ($q = 1, a = b, m = 5, n_1 = 1/2, n_2 = n_3 = 4/3$): (a) optics axis pattern; (b) the phase profile imparted by the SVAP to an input beam; (c) a microscope image of the SVAP between crossed polarizers; (d) a microscope image of the SVAP between crossed polarizers+ and a birefringent compensator plate at 45° . This image unveils the optic axis pattern underlying the SVAP (a). The image has been recorded by illuminating the sample with white light, sandwiched between crossed polarizers, and inserting, between the sample and the analyzer, a birefringent λ -compensator ($\lambda = 550$ nm), with the optic axis rotated by 45° . The arrows in the lower left corner sketch the axes orientations of the input linear polarizer (black arrow), the output analyzer (red arrow) and the λ -compensator (blue arrow) [45].

Figure 4 shows the OAM power spectrum $|c_l|^2$ for FFH₁⁵ (figure 4(a)) and FFH_{1/2}⁶ (figure 4(b)). In classical optics, the quantity $|c_l|^2$ is the fraction of the total power of the optical field component carrying an OAM proportional to l . In quantum optics, it is the probability that a photon in the beam carries an OAM of $\hbar l$. The actual values of $|c_l|^2$ have been determined numerically.

Comparing the wavefronts in figures 1(b) and 2(b), we clearly see that the primrose modulation is weaker than the starfish's. This is consistent with the fact that the starfish OAM spectrum (centered around $l = -3$) is broader than the primrose one (centered around $l = 1$). This is mainly due to the value of the indices $n_2 = n_3 = 2.3$ characterizing the primrose beam profile, which is close to the critical value $n_2 = n_3 = 2$ corresponding to having a uniform profile with no modulation.

In figures 5(a) and 6(a), we show the optic axis patterns of the SVAPs used for generating starfish and primrose modes, respectively. Figure 5(c) shows a microscope image of the starfish SVAP between crossed polarizers, while figure 5(d) displays a similar microscope image obtained with a birefringent λ -compensator inserted between the SVAP and the analyzer. The λ -compensator has a path difference of 550 nm and therefore introduces a π retardation at that wavelength. The fast axis forms a 45° angle to the axis of the analyzer. When the compensator is put in, the sample changes its color depending on its orientation. The changes in color are based on optical interference. This method fully unveils the optic axis pattern underlying the SVAP (figure 5(a)), because, unlike the simple crossed-polarizers method, it enables one to distinguish between orthogonal orientations of the optic axis. Similar remarks apply to figure 6.

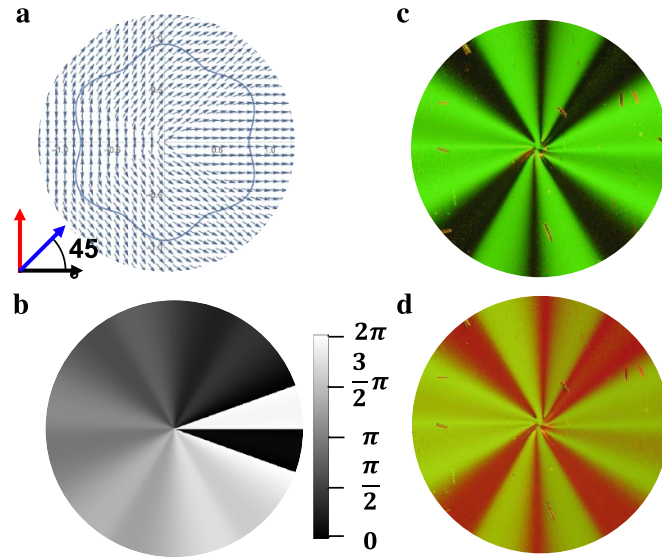


Figure 6. Experimental observation of the optic axis distribution of the water primrose SVAP ($q = 1/2$, $a = b$, $m = 6$, $n_1 = 2/3$, $n_2 = n_3 = 2.3$): (a) optics axis pattern; (b) the phase profile imparted by the SVAP to an input beam; (c) a microscope image of the SVAP between crossed polarizers; (d) a microscope image of the SVAP between crossed polarizers+ and a birefringent compensator plate at 45° . This image unveils the optic axis pattern underlying the SVAP (a). The image has been recorded by illuminating the sample with white light, sandwiched between crossed polarizers, and inserting, between the sample and the analyzer, a birefringent λ -compensator ($\lambda = 550$ nm), with the optic axis rotated by 45° . The arrows in the lower left corner sketch the axes orientations of the input linear polarizer (black arrow), the output analyzer (red arrow) and the λ -compensator (blue arrow) [45].

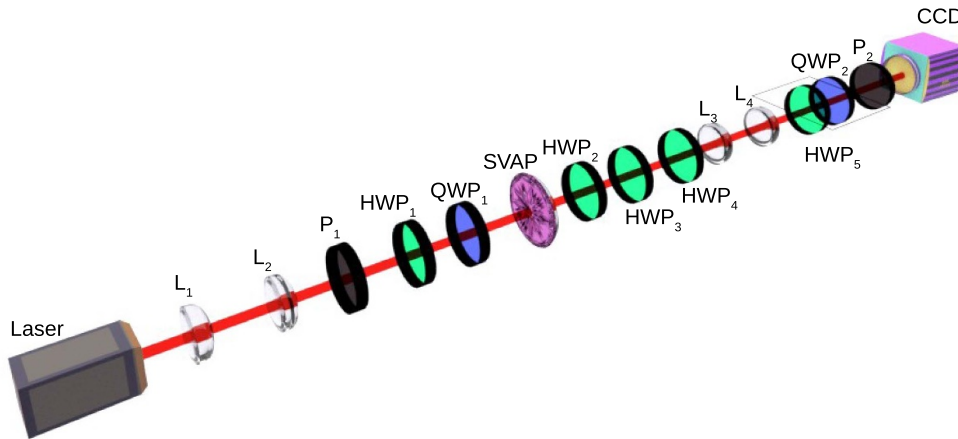


Figure 7. The experimental setup for spatially-resolved polarimetric measurements. A telescope including the lenses L_1 and L_2 expands the light beam from a He–Ne laser source ($\lambda = 632.8$ nm, maximum power output $P_o = 5$ mW, beam waist $w_0 = 0.5$ mm). The linear polarizer P_1 and the QWP_1 are used to make the input polarization circular. The latter is replaced with a half-waveplate HWP_1 when the input polarization is linear horizontal or vertical. A pair of half-waveplates, HWP_2 and HWP_3 , have been inserted to precisely set the phase angle $\alpha = 0$ in equation (1). A half-waveplate HWP_4 is used for swapping left-/right-handed circular polarized output states, when needed. The SVAP, the lenses L_3 and L_4 , and the CCD camera are positioned in the $4f$ configuration for near-field measurements. A single lens is adopted for far-field measurements. The half-waveplate HWP_3 , the quarter-waveplate QWP_2 and the linear polarizer P_2 are used to measure the local Stokes parameters over the wavefront.

4.2. MPBs and polarization singularities

Exploitation of the starfish and primrose SVAPs, exotic MPBs and corresponding polarization singularities can be realized. As mentioned, V-points are generated by setting the SVAP retardation to $\delta = \pi$ (half-waveplate operation mode) and using a linearly polarized Gaussian input beam. Similarly, C-points are generated by setting the SVAP retardation to

$\delta = \pi/2$ (quarter-waveplate operation mode), using a circularly polarized input and, when required, swapping the output handedness with an output half-waveplate.

The various resulting polarization patterns have been experimentally generated and observed using the optical setup sketched in figure 7. Polarization patterns have been observed both in the near field (figure 8 for starfish MPBs and figure 9 for primrose MPBs) and in the far field (figure 10 for

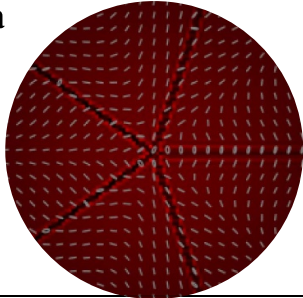
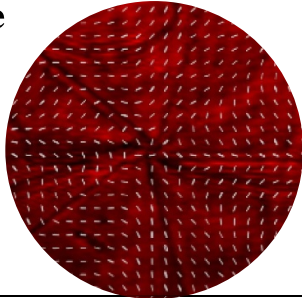
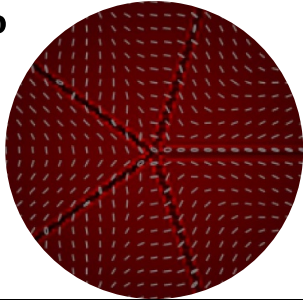
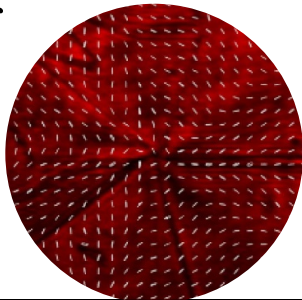
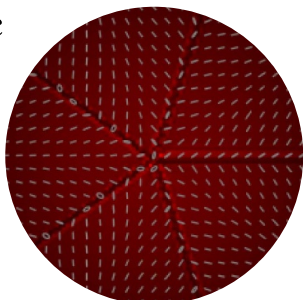
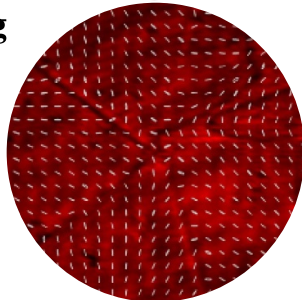
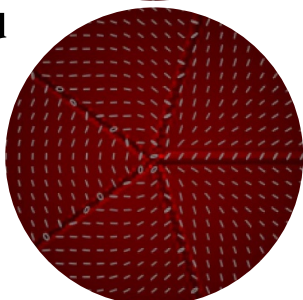
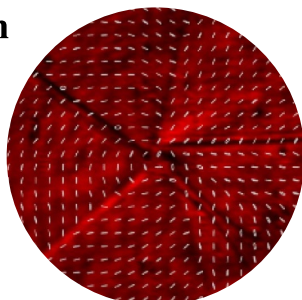
δ	$ p_0\rangle$	HWP ₄	Theoretical predictions	Experimental results
π	$ H\rangle$	N	a 	e 
π	$ V\rangle$	N	b 	f 
$\frac{\pi}{2}$	$ L\rangle$ $ R\rangle$	N	c 	g 
$\frac{\pi}{2}$	$ L\rangle$ $ R\rangle$	Y	d 	h 

Figure 8. Near-field polarization patterns and transverse intensity distribution of starfish Poincaré beams. Theoretical predictions and experimental results for different retardation values δ and different input polarization states $|p_0\rangle$. For each configuration, the presence/absence of HWP₄ is specified with the label Y/N, respectively. Axial V-points occur in the 1st and 2nd rows (a), (e) and (b), (f), corresponding to predominantly radial and azimuthal patterns, respectively. Axial C-points occur in the 3rd and 4th rows (c), (g) and (d), (h), corresponding to lemon-like and star-like patterns, respectively.

starfish MPBs and figure 11 for primrose MPBs). Experimental findings quite satisfactorily match the theoretical predictions, shown aside for comparison purposes. Specifically, the agreement between the experimental polarization pattern in figure 10(h) and the theoretical prediction in figure 10(d) is very satisfactory over the bright central spot of the far-field beam transverse cross section, but it is less good in the surrounding region. We ascribe this to the low experimental

signal-to-noise ratio in the outer region of the image. Generally speaking, discrepancies between theoretical and experimental profiles are ascribed to residual asymmetries in the fabricated SVAPs and to the limited accuracy in the central singularity manufacturing.

Near-field observations confirm that an SVAP operated as a quarter-waveplate imparts to a circularly polarized input beam an inhomogeneous polarization pattern replicating its

δ	$ p_0\rangle$	HWP ₄	Theoretical predictions	Experimental results
π	$ H\rangle$	N	a	e
π	$ V\rangle$	N	b	f
$\frac{\pi}{2}$	$ L\rangle$ $ R\rangle$	N	c	g
$\frac{\pi}{2}$	$ L\rangle$ $ R\rangle$	Y	d	h

Figure 9. Near-field polarization patterns and transverse intensity distribution of primrose Poincaré beams. Theoretical predictions and experimental results for different retardation values δ and different input polarization states $|p_0\rangle$. For each configuration, the presence/absence of HWP₄ is specified with the label Y/N, respectively. Axial V-points occur in the 1st and 2nd rows (a), (e) and (b), (f), corresponding to predominantly radial and azimuthal patterns, respectively. Axial C-points occur in the 3rd and 4th rows (c), (g) and (d), (h), corresponding to lemon-like and star-like patterns, respectively.

axis distribution: compare figures 8(c) and (g) with figure 5(a) and figures 9(c) and (g) with figure 6(a). Far-field observations support the conclusion that the primrose modulation is weak, since the several polarization patterns observed return the radial, azimuthal, lemon and star configurations typical of Poincaré beams generated using uniform helical modes with $\ell = 1$. Poincaré beams generated using starfish modes, in

contrast, significantly deviate from their uniform counterparts with $\ell = 2$.

In particular, in the latter case, ‘fault’ radial lines of sharply reduced intensity appear in the optical field, owing to the presence of discontinuities in the azimuthal phase of the FFH modes (cusps in the superformula). Such lines already arise in the scalar wavefront, independently of polarization

δ	$ p_0\rangle$	HWP ₄	Theoretical predictions	Experimental results
π	$ H\rangle$	N	a	e
π	$ V\rangle$	N	b	f
$\frac{\pi}{2}$	$ L\rangle$ $ R\rangle$	N	c	g
$\frac{\pi}{2}$	$ L\rangle$ $ R\rangle$	Y	d	h

Figure 10. Far-field polarization patterns and transverse intensity distribution of starfish Poincaré beams. Theoretical predictions and experimental results for different retardation values δ and different input polarization states $|p_0\rangle$. For each configuration, the presence/absence of HWP₄ is specified with the label Y/N, respectively. Axial V-points occur in the 1st and 2nd rows (a), (e) and (b), (f), corresponding to predominantly radial and azimuthal patterns, respectively. Axial C-points occur in the 3rd and 4th rows (c), (g) and (d), (h), corresponding to lemon-like and star-like patterns, respectively.

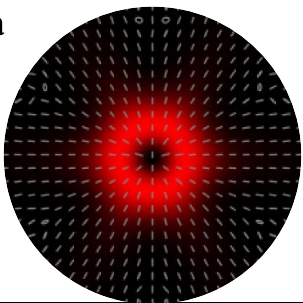
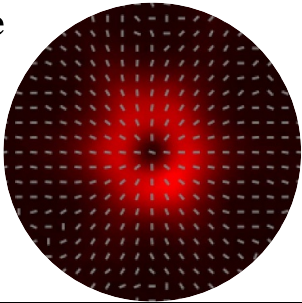
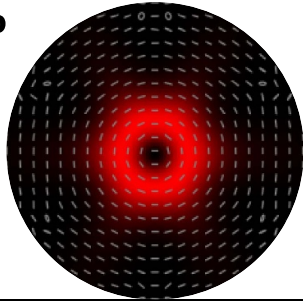
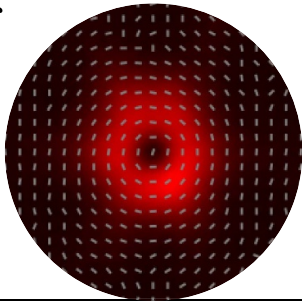
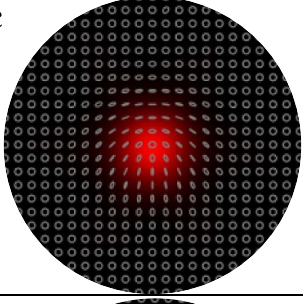
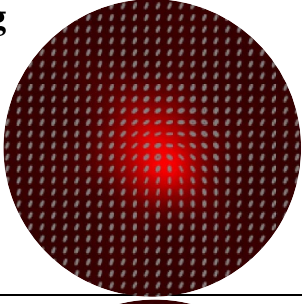
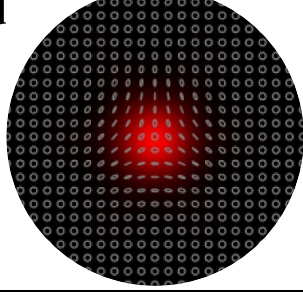
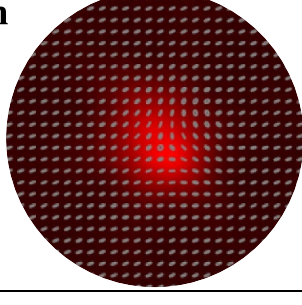
δ	$ p_0\rangle$	HWP ₄	Theoretical predictions	Experimental results
π	$ H\rangle$	N	a 	e 
π	$ V\rangle$	N	b 	f 
$\frac{\pi}{2}$	$ L\rangle$ $ R\rangle$	N	c 	g 
$\frac{\pi}{2}$	$ L\rangle$ $ R\rangle$	Y	d 	h 

Figure 11. Far-field polarization patterns and transverse intensity distribution of primrose Poincaré beams. Theoretical predictions and experimental results for different retardation values δ and different input polarization states $|p_0\rangle$. For each configuration, the presence/absence of HWP₄ is specified with the label Y/N, respectively. Axial V-points occur in the 1st and 2nd rows (a), (e) and (b), (f), corresponding to radial and azimuthal patterns, respectively. Axial C-points occur in the 3rd and 4th rows (c), (g) and (d), (h), corresponding to lemon and star patterns, respectively.

inhomogeneities, and consequently they are deeply different in nature from the L-lines commonly observed in polarization patterns. These intensity fault lines turn out to be more or less pronounced according to the strength of the phase modulation and are preserved, although smoothed out, on free space propagation.

5. Conclusions

We have introduced a wide class of inhomogeneously polarized optical beams obtained as inseparable superpositions of left/right-handed circular polarization states and FFH modes. Such beams, dubbed MPBs, are obtained by combining an azimuthal phase modulation with a uniform helical one. The phase modulation is selected on the grounds of a geometric approach enabling one to transfer geometric properties of a closed plane curve to the azimuthal phase of a paraxial light beam. Specifically, the rate of change of the curvature is translated into the azimuthal rate of change of the optical phase. Experimental generation of such beams can be advantageously, although not exclusively, achieved by using electrically-tunable spatially varying axis retardation waveplates based on LCs. Such SVAPs have the remarkable property of translating their optic axis pattern into polarization distribution when operated as quarter-waveplates with an input circularly polarized beam.

As examples of such beams, we have generated and characterized intensity distributions and polarization singularities of two distinct groups of MPBs, which differ in topological charge, rotational symmetry and strength of phase modulation. We think that MPBs can be of help in exploring and mastering a wider class of polarization singularities potentially relevant in both fundamental and applied optics. MPBs can certainly be used as a more flexible option to ordinary Poincaré beams in all their currently investigated applications. In particular, they could find applications in the optical manipulation of micro-particles, such as in the control of polarotactic natural or artificial microswimmers [13].

Data availability statement

The data that support the findings of this study are available upon reasonable request from the authors.

Acknowledgment

This work was supported by the European Union (EU) within Horizon 2020—European Research Council Advanced Grant No. 694683 (PHOSPhOR). and by University of Naples Research Funding Program (DR no. 3425-10062015).

ORCID iDs

Verónica Vicuña-Hernández  <https://orcid.org/0000-0002-6926-8772>

Lorenzo Marrucci  <https://orcid.org/0000-0002-1154-8966>
Ester Piedipalumbo  <https://orcid.org/0000-0001-8468-4953>
Bruno Piccirillo  <https://orcid.org/0000-0002-1517-6899>

References

- [1] Cronin T W, Shashar N, Caldwell R L, Marshall J, Cheroske A G and Chiou T H 2003 *Integr. Comp. Biol.* **43** 549–58
- [2] Shi X q and Ma Y q 2013 *Nat. Commun.* **4** 3013
- [3] Machon T and Alexander G P 2014 *Phys. Rev. Lett.* **113** 027801
- [4] Isaeva V V, Kasyanov N V and Presnov E V 2012 *Biosystems* **109** 280–98
- [5] Vitelli V, Jain B and Kamien R D 2009 *J. Cosmol. Astropart. Phys.* **2009** 034
- [6] Nye J F 1999 *Natural Focusing and Fine Structure of Light: Caustics and Wave Dislocations* (Bristol: Institute of Physics Publishing)
- [7] Cardano F and Marrucci L 2015 *Nat. Photon.* **9** 776–8
- [8] D'Errico A, Maffei M, Piccirillo B, de Lisio C, Cardano F and Marrucci L 2017 *Sci. Rep.* **7** 40195
- [9] Mawet D, Serabyn E, Liewer K, Burruss R, Hickey J and Shemo D 2009 *Astrophys. J.* **709** 53–7
- [10] Piccirillo B, Piedipalumbo E, Marrucci L and Santamato E 2019 *Mol. Cryst. Liq. Cryst.* **684** 15–23
- [11] Dorn R, Quabis S and Leuchs G 2003 *Phys. Rev. Lett.* **91** 233901
- [12] Abouraddy A F and Toussaint K C 2006 *Phys. Rev. Lett.* **96** 153901
- [13] Yang S, Huang M, Zhao Y and Zhang H P 2021 *Phys. Rev. Lett.* **126** 058001
- [14] Shvedov V, Davoyan A R, Hnatovsky C, Engheta N and Krolikowski W 2014 *Nat. Photon.* **8** 846–50
- [15] Rui G, Wang X, Gu B, Zhan Q and Cui Y 2016 *Opt. Express* **24** 7212–23
- [16] Anoop K K, Rubano A, Fittipaldi R, Wang X, Paparo D, Vecchione A, Marrucci L, Bruzzese R and Amoroso S 2014 *Appl. Phys. Lett.* **104** 241604
- [17] Li X, Lan T H, Tien C H and Gu M 2012 *Nat. Commun.* **3** 998
- [18] Neugebauer M, Bauer T, Banzer P and Leuchs G 2014 *Nano Lett.* **14** 2546–51 (PMID: 24724814)
- [19] D'Ambrosio V, Nagali E, Walborn S P, Aolita L, Slussarenko S, Marrucci L and Sciarrino F 2012 *Nat. Commun.* **3** 961
- [20] Fickler R, Lapkiewicz R, Ramelow S and Zeilinger A 2014 *Phys. Rev. A* **89** 060301
- [21] Cardano F, Maffei M, Massa F, Piccirillo B, de Lisio C, De Filippis G, Cataudella V, Santamato E and Marrucci L 2016 *Nat. Commun.* **7** 11439
- [22] Frederick N J 1983 *Proc. R. Soc. A* **389** 279–90
- [23] Hajnal V J 1987 *Proc. R. Soc. A* **414** 433–46
- [24] Hajnal V J 1987 *Proc. R. Soc. A* **414** 447–68
- [25] Berry M V 2004 *J. Opt. A: Pure Appl. Opt.* **6** 475–81
- [26] Berry M V and Dennis M R 2001 *Proc. R. Soc. Lond. A* **457** 141–55
- [27] Kumar Pal S, Ruchi and Senthilkumaran P 2017 *Opt. Commun.* **393** 156–68
- [28] Senthilkumaran P 2018 *Singularities in Physics and Engineering* (Bristol: IOP Publishing) pp 2053–563
- [29] Beckley A M, Brown T G and Alonso M A 2010 *Opt. Express* **18** 10777–85
- [30] Galvez E J, Khadka S, Schubert W H and Nomoto S 2012 *Appl. Opt.* **51** 2925–34

- [31] Maurer C, Jesacher A, FÜRhapter S, Bernet S and Ritsch-Marte M 2007 *New J. Phys.* **9** 78
- [32] Freund I 2002 *Opt. Commun.* **201** 251–70
- [33] Cvarch B A, Khajavi B, Jones J A, Piccirillo B, Marrucci L and Galvez E J 2017 *Opt. Express* **25** 14935–43
- [34] Galvez E J, Rojec B L and Cheng X 2013 Polarization singularities in Poincare' optical beams *The Rochester Conferences on Coherence and Quantum Optics and the Quantum Information and Measurement Meeting* (Optical Society of America) p M2A.3
- [35] Freund I 2011 *Opt. Commun.* **284** 3816–45
- [36] Khajavi B and Galvez E J 2016 *J. Opt.* **18** 084003
- [37] Niv A, Biener G, Kleiner V and Hasman E 2005 *Opt. Lett.* **30** 2933–5
- [38] Beresna M, Gecevičius M, Kazansky P G and Gertus T 2011 *Appl. Phys. Lett.* **98** 201101
- [39] Kumar V and Viswanathan N K 2013 *Opt. Lett.* **38** 3886–9
- [40] Vyas S, Kozawa Y and Sato S 2013 *Opt. Express* **21** 8972–86
- [41] Moreno I, Davis J A, Cottrell D M and Donoso R 2014 *Appl. Opt.* **53** 5493–501
- [42] Otte E, Alpmann C and Denz C 2016 *J. Opt.* **18** 074012
- [43] Cardano F, Karimi E, Marrucci L, de Lisio C and Santamato E 2013 *Opt. Express* **21** 8815–20
- [44] Piccirillo B, Slussarenko S, Marrucci L and Santamato E 2013 *Riv. Nuovo Cimento* **36** 501–55
- [45] Piccirillo B, Piedipalumbo E and Santamato E 2020 *Frontiers Phys.* **8** 94
- [46] Cardano F, Karimi E, Slussarenko S, Marrucci L, de Lisio C and Santamato E 2012 *Appl. Opt.* **51** C1–6
- [47] Gielis J 2003 *Am. J. Bot.* **90** 333–8
- [48] Sokolov D 2001 *Lamé curves Encyclopedia of Mathematics*, ed M Hazewinkel (Berlin: Springer Science+Business Media B.V./Kluwer Academic Publishers)
- [49] Piccirillo B, D'Ambrosio V, Slussarenko S, Marrucci L and Santamato E 2010 *Appl. Phys. Lett.* **97** 241104
- [50] Alemán-Castaneda L A, Piccirillo B, Santamato E, Marrucci L and Alonso M A 2019 *Optica* **6** 396–9
- [51] Rubano A, Cardano F, Piccirillo B and Marrucci L 2019 *J. Opt. Soc. Am. B* **36** D70–87